ORIGINAL ARTICLE

Nanostructured AlNiCoFeCrTi high-entropy coating performed by cold spray

D. V. Hushchyk[1] · A. I. Yurkova[1] · V. V. Cherniavsky[1] · I. I. Bilyk[1] · S. O. Nakonechnyy[1]

Abstract

In this work, solid-state mechanical alloying (MA) and cold spraying (CS) processes were applied to fabricate powder AlNiCoFeCrTi high-entropy alloy (HEA) and then to produce HE coatings on steel substrate. Shot-time MA for 3 h has been employed to synthesize nanostructured equiatomic AlNiCoFeCrTi HEA of metastable supersaturated substitutional solid solution with bcc crystal structure. Although alloying is not complete at this shot milling time, it goes to completion during thermal annealing to achieve the alloy formation. XRD study on mechanically alloyed high-entropy AlNiCoFeCrTi alloy after thermal annealing at 1200 °C for 1 h revealed the formation of a three-phase structure consisting of ordered bcc phase with fine precipitates of intermetallic σ-phase (FeCr) and titanium carbide TiC. The powder agglomerates resulted from annealing were grinded in a ball mill for 1 h. Nanostructured disordered bcc solid solution, TiC and σ-phases are noticed after milling. Coatings of 450 μm in mean thickness were deposited by the CS process using an air like a working gas, temperature and pressure of 450 °C and 0.9 MPa, respectively. The experimental results confirm that CS process can be used to produce HE coatings with low porosity. As a low-temperature deposition process, CS completely retained the HEA phase composition and nanostructure in the coating without any phase transformation. The AlFeNiCoCrTi HE coatings exhibit 10.3 ± 0.3 GPa in Vickers hardness.

Keywords High-entropy alloy · Mechanical alloying · Nanostructure · Phase transformation · Cold spray · Coating

Introduction

In many situations, only the contact surface properties are important in determining performance of the component in practical applications. Therefore, the use of coatings from materials with high physical and mechanical characteristics, such as high-entropy alloys (HEAs) (Murty et al. 2014; Tsai et al. 2014; Gao et al. 2016; Ye et al. 2016; Miracle et al. 2017), has several attractive advantages. HEAs are a new generation alloys and are quite different from traditional alloys, which are based on one or two elements. HEAs are typically defined as multicomponent alloys whose principal elements are at least five in equiatomic or near equiatomic ratio, and the concentration of each constituent element is between 5 and 35 at. % (Murty et al. 2014; Gao et al. 2016; Miracle et al. 2017). HEAs have been found to have novel

microstructures and unique properties. At the same time, by controlling the composition of HEA, it is possible to achieve high hardness, wear resistance, corrosion and oxidation resistance, high temperature performance (Yeh et al. 2007a, b; Murty et al. 2014; Gao et al. 2016). Therefore, due to their superior properties over conventional metals and alloys, HEAs are great candidates for coating materials.

The production of HEAs does not require special processing equipment; so, the manufacturing of HEAs can be easily realized with existing technologies and equipment (Tsai et al. 2014; Gao et al. 2016). Nowadays, the primary method to synthesize HEAs is vacuum arc remelting for bulk cast ingot; mechanical alloying followed by isostatic pressing and surface coating is also possible (Murty et al. 2014; Gao et al. 2016; Alaneme et al. 2016). HEA coatings were mainly produced using fusion-based technologies, such as laser cladding (Alaneme et al. 2016; Zhang et al. 2017), plasma cladding (Dong et al. 2013; Cai et al. 2017a, b), plasma spraying (Wang et al. 2011; Alaneme et al. 2016) and magnetron sputtering (Chang 2018; Zhang et al. 2018). However, melting and solidification commonly result in

✉ D. V. Hushchyk
d.hushchyk@gmail.com

[1] National Technical University of Ukraine "Igor Sikorsky Kyiv Polytechnic Institute", Kyiv, Ukraine

مدينة الملك عبدالعزيز
للعلوم والتقنية KACST

🙂 Springer

phase transformation and element segregation of the HEA coatings, breaking the nature of HEAs (Cai et al. 2017a, b). So, it is significant to use a non-fusion-based coating technology to prevent the phase and structure transformation of HEAs during coating formation.

Considering HEA's tendency to form simple structures, fabricating HEA coating by solid-state processes such as mechanical alloying (MA) and cold spraying (CS) is of great significance and potential for wide use.

MA is a widely used high-energy solid-state processing route for the synthesis of advanced materials (Suryanarayana 2001; Vaidya et al. 2019). The extension of solid solubility with good homogeneity and room-temperature processing are the main advantages of MA over the casting route associated with segregation problems and inhomogeneity, especially with multicomponent systems with large differences in the melting points (Varalakshmi et al. 2010; Murty et al. 2014; Gao et al. 2016; Alaneme et al. 2016; Yurkova et al. 2016, 2019; Vaidya et al. 2019). Furthermore, MA route is also established to facilitate the formation of nanocrystalline HEA with superior properties (Varalakshmi et al. 2010; Alaneme et al. 2016; Yurkova et al. 2016, 2019; Vaidya et al. 2019).

Cold gas dynamic spraying or cold spraying is rather novel and promising technology to obtain surface coatings (Alkhimov et al. 1994; Papyrin et al. 2007), offering several technological advantages over thermal spray since it utilizes kinetic rather than thermal energy for deposition. As a result, residual thermal stresses, phase transformation, oxidation and undesired chemical reactions can be avoided. The development of new material systems with enhanced properties covering a wide range of required functionalities of surfaces and interfaces brought forth new opportunities to the CS with a rich variety of material combinations. CS has emerged as a promising process to deposit nanostructured materials without significantly changing their structure and phase composition whereas many traditional consolidation processes do (Papyrin et al. 2007; Moridi et al. 2014). The technology of cold spraying is a promising way to protect, repair and restore parts.

In the CS process, high-temperature compressed gases (typically air, nitrogen, or helium) are used as the propulsive gas to accelerate powder feedstock (typically metals and metal matrix composites) to a high velocity (typically higher than 300 m/s), and to induce deposition when the powder particles impact onto a substrate. In contrast to conventional high-temperature deposition processes, the adhesion of particles in CS process is due solely to their kinetic energy upon impact rather than the thermal energy (Papyrin et al. 2007; Moridi et al. 2014; Yin et al. 2018a, b). The feedstock used for CS remains solid state during the entire deposition process. Deposition is achieved through local metallurgical bonding and mechanical interlocking which are caused by localized severe plastic deformation at the particle–substrate and inter-particle interfaces. This allows for the avoidance of defects commonly encountered in high-temperature deposition processes, such as oxidation, residual thermal stress and phase transformation (Li et al. 2012; Rokni et al. 2017; Raoelison et al. 2018).

Experimental investigations show that successful bonding is achieved only above a critical particle velocity, whose value depends on the temperature and the thermomechanical properties of the sprayed material (Stoltenhoff et al. 2002; Papyrin et al. 2007; Moridi et al. 2014). The analysis demonstrates that bonding can be attributed to adiabatic shear instabilities (Assadi et al. 2003; Grujicic et al. 2004) which occur at the particle surface at or beyond the critical velocity. On the basis of this criterion, critical velocities can be predicted and used to optimize process parameters for various materials (Assadi et al. 2003; Grujicic et al. 2004).

CS has been successfully used to deposit different materials such as metals, alloys ceramics, composites and polymers (Moridi et al. 2014; Watson et al. 2017), showing facilities in producing high-entropy alloy coatings. Until now, this method for preparing HEA coatings has just been reported only in (Yin et al. 2018a, b; Anupam et al. 2019).

This study reports the structural evolution of equiatomic high-entropy AlNiCoFeCrTi alloy from elemental materials to metastable solid solution during mechanical alloying (MA) and then to equilibrium phases during subsequent thermal annealing and further to coatings during cold-spraying process. The microhardness of the coatings was also investigated.

Experimental procedures

Materials and processing

Feedstock nanostructured powder of high-entropy alloy with nominal composition of AlFeNiCoCrTi was chosen for experimentations and fabricated by shot-time mechanical alloying (MA) within 3 h using planetary ball mill and subsequent thermal annealing at temperature 1200 °C during 1 h. Hardened steel vial and balls were used as a grinding media and petrol was used as a process controlling agent. The powder agglomerates formed after annealing of AlFeNiCoCrTi HEA were subjected to grinding in a ball mill for 1 h.

Deposition of powder AlFeNiCoCrTi high-entropy alloy was performed by CS process on a steel substrate using an air with a gun temperature and pressure of 450 °C and 0.9 MPa, respectively. The stand-off distance between the nozzle and the steel substrate was 30 mm. A commercial cold spray system (DYMET 405) was used in spraying experiments with compressed air. Cold-sprayed principle

and technical set-up for cold spraying are described elsewhere in more detail (Alkhimov et al. 1994; Papyrin et al. 2007; Moridi et al. 2014). A cold rolled plate of low carbon steel (carbon content 0.2%) with a thickness about 3.0 mm was used as a substrate. Immediately prior to depositing the coatings, the substrate surface was prepared by SiC-blasting, rinsing, and then wiping with solvent to eliminate surface wetness. Finally, coatings with mean thickness about 450 μm were obtained for further experiments.

Structural characterization

The effects of milling duration (1, 2, 3 h), subsequent annealing at temperature of 1200 °C and consolidation by CS process of as-MA alloy on the crystalline structure and phase transformation were investigated by means of Rigaku Ultima IV X-ray diffractometer with Cu Kα radiation and the working voltage and current were 30 kV and 20 mA, respectively. The range of scanning angle (2θ) was from 20° to 120°. The scanning step was 0.04° with an angular speed of the goniometer rotation of 1°/min. The lattice parameters of solid solutions were calculated according to the positions of the gravitation centers of the diffraction profiles by linear extrapolation method. The crystallite size (coherent-scattering region) in the milled powders as well as after consolidation by CS process has been calculated from the XRD peak broadening using peak profile analysis after eliminating the instrumental and strain contributions.

Scanning electron (SEM) microscope equipped by X-ray detector (EDX) was used to recognize as-milled and as-annealed powder particle morphology (size and shape) and microstructure, as well as to get basic information about particle/particle bonding achieved in cold-sprayed coating and also to measure the chemical composition of materials.

The particle size distribution was determined by Microtrac-Turbo Sync. The Sync interrogated wet particles with laser light; while, simultaneously, a high-speed digital camera took images. Samples were introduced to the FlowSync and dispersed throughout the system. Scattered light was captured with laser sequence across 165 degrees. Simultaneously, live images of the sample were taken with a high-speed digital camera. (Microtrac S3500 2011).

Mechanical testing

The room-temperature microhardness measurements were performed from the metallographic cross sections using a conventional microhardness machine Digital Microhardness Tester MHV-1000 equipped by standard Vickers' pyramid. Microhardness numbers were determined under indentation load as high as 1.0 N and duration time of 15 s. Each coating was tested for multipoints from the surface to the interface with an equal interval of about 30 μm.

Thermodynamic parameters to predict the phase formation

For multi-component alloys, it is important to predict the combined effect of the alloying elements on the phase formation attributed to a competition between the formation of different solid solutions and other phases, for instance, intermetallics. HEAs have tendency to form solid solution phases as compared with intermetallic compounds, which is ascribed to their enhanced configurational entropy of mixing ΔSconfig (Murty et al. 2014; Tsai et al. 2014; Gao et al. 2016; Vaidya et al. 2019). However, as more and more HEAs are being studied, it has been found that configurational entropy is not alone sufficient to stabilize the solid solution (Zhang et al. 2008; Guo et al. 2011; Tsai et al. 2014; Gao et al. 2016; Miracle et al. 2017; Pickering and Jones 2016; Vaidya et al. 2019).

It is known that the formation of simple or complex phases in HEAs depends mainly on the entropy of mixing ΔS_{mix}, enthalpy of mixing ΔH_{mix}, and atomic size differences or size factor, δ (Zhang et al. 2008; Guo et al. 2011; Murty et al. 2014; Tsai et al. 2014; Gao et al. 2016; Ye et al. 2016; Miracle et al. 2017). To form only simple ordered/disordered phases (i.e., fcc, bcc, and their mixtures), the following conditions have to be satisfied simultaneously: $11 \leq \Delta S_{\text{mix}} \leq 19.5$ J/(mol K), $-22 \leq \Delta H_{\text{mix}} \leq 7$ kJ/mol, and $\delta \leq 8.5$ (Guo et al. 2011). The entropy of mixing ΔS_{mix} has to be large enough because it is the main stabilizing factor for simple phases. The enthalpy of mixing ΔH_{mix} cannot be too large in value because large positive ΔH_{mix} leads to phase separation and large negative parameter ΔH_{mix} typically leads to intermetallic phases. Size factor δ has to be small enough since large value of parameter δ leads to excess strain energy and destabilizes simple structures. If phase composition is limited to solid disordered phases only, the conditions are more severe: $12 \leq \Delta S_{\text{mix}} \leq 17.5$ J/(mol K), $-15 \leq \Delta H_{\text{mix}} \leq 5$ kJ/mol, and parameter $\delta \leq 4.3\%$ (Tsai et al. 2014; Yin et al. 2018a, b).

One of the most critical factors that decides whether an alloy crystallizes into bcc or fcc structure appears to be its average valence electron concentration (VEC) (Tsai et al. 2014; Miracle et al. 2017; Guo et al. 2011). It was found that when the VEC of the alloy is smaller than 6.87, the bcc structure is stabilized (Guo et al. 2011). When the VEC of the alloy is larger than 8, the fcc structure is stabilized. Coexistence of bcc and fcc phases is observed at VEC values between 6.87 and 8 (Guo et al. 2011).

Moreover, the tendency of getting simple solid solution phases is higher during MA of HEAs. MA process has been shown to extend solid solubility even in immiscible systems because of the nanostructure formation during milling (Murty and Ranganathan 1998; Suryanarayana et al. 2001; Vaidya et al. 2019). The large volume fraction of atoms in

the grain boundaries in these ultrafine-grained materials is expected to enhance diffusion and consequently increase the solid solubility (Suryanarayana et al. 2001). Further, it is also possible to achieve supersaturation in some alloy systems by MA that is not possible by other technique and this is especially true in liquid immiscible systems (Suryanarayana 2001). Therefore, the tendency of solid solution phases formation is enhanced during MA of HEAs.

The values of thermodynamic parameters for t the alloy system under study (AlNiCoFeCrTi) are listed in Table 1. These parameters were calculated from the formulas proposed in (Guo et al. 2011; Tsai et al. 2014; Murty et al. 2014; Gao et al. 2016; Yurkova et al. 2016; Vaidya et al. 2019):

As summarized in Table 1, we can conclude that the AlNiCoFeCrTi HEA besides bcc solid solution could contain intermetallic compounds because of large negative enthalpy. However, in many cases, the parametric approaches can only predict the phases formed during MA and thermal treatment.

Results and discussions

Structure evolution of elemental powders during mechanical alloying

Figure 1 represents the XRD patterns of AlNiCoFeCrTi alloy as a function of milling time. The pattern of 0 h exhibits peaks of all the pure elements in the initial blend. It can be seen that as milling time increases, drastic decrement of diffraction intensity and peak broadening are observed. The peak intensity decreases dramatically in the early stages of milling after the powder was grinded for 1 h. Obvious peaks broadening can be observed and a lot of peaks become invisible with an increase in grinding time. The disappearance of diffraction peaks can be seen as the beginning of the solid solution formation. Only the most intense diffraction peaks can be clearly seen in the 2-h ball-milled powder, which indicates the formation of
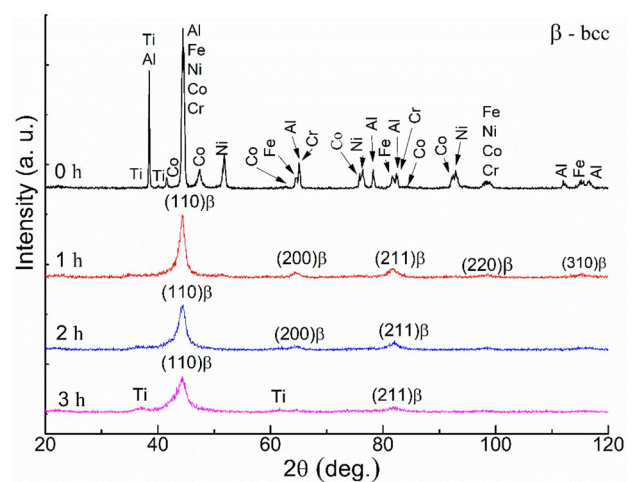

Fig. 1 XRD patterns of equiatomic AlFeNiCoCrTi powders with different milling times

the single-phase disordered solid solution with body-centered cubic (bcc) structure (β-phase). As the milling time reaches up to 3 h, the diffraction peaks exhibit no changes except for a minor broadening. The intensity decrement and peak broadening in the diffraction can be attributed to the formation of nanostructure and high lattice strain induced by severe plastic deformation during the MA process (Yeh et al. 2007a, b; Yurkova et al. 2016, 2019; Vaidya et al. 2019).

However, the cause of diffraction peak disappearance is complicated, which can be introduced by particle and crystal refinement together with high lattice strain, different atomic diffraction factor proportional to the atomic number, crystallinity decrement, formation of solid solution. For the XRD peak intensity, the distorted atomic planes increase X-ray diffuse scattering effect and give smaller peak intensity (Yeh et al. 2007a, b). Most of the diffraction peaks can hardly be seen after ball milled for 3 h. Thus, the formation of nanocrystalline and high lattice strain are primary factors of the above-mentioned broadening and decrement of diffraction intensity of the diffraction peaks. Moreover, size mismatch effect between the constituents, increasing grain boundary fraction and increasing dislocation density produced by severe plastic deformation under ball milling lead to the increment of lattice strain (Yeh et al. 2007a, b; Vaidya et al. 2019).

Only broaden diffraction peaks corresponding to the disordered bcc solid solution, and residual pure titanium, which is not completely dissolved in bcc solid solution, are observed in the XRD pattern of AlFeNiCoCrTi alloy after 3-h MA. So, complete solubility of Ti is not observed in AlNiCoFeCrTi after 3-h MA.

The titanium has the largest atomic radius among the alloy components; therefore, in a short time MA process

Table 1 Solid solution criteria parameter values for multi-principle elemental AlNiCoFeCrTi HEA

HEA	Entropy of mixing, ΔS_{mix} (J/ mol K)	Enthalpy of mixing, ΔH_{mix} (kJ/mol)	Atomic size difference, δ (%)	Valence electron concentration, VEC (e/ at)	Phase composition
AlNiCo-FeCrTi	14.87	− 21.38	7.25	6.64	bcc, intermetallic compounds

does not completely dissolve, so weak diffraction peaks corresponding to residual pure Ti are visible in the XRD patterns.

The lattice constant of disordered bcc solid solution (β-phase) is estimated to be 0.2884 nm by linearity extrapolation method. The crystallite size of the alloy powders under different milling times has been calculated from the X-ray peak broadening using Scherrer's formula after eliminating the instrumental contribution. The mean crystallite size of the alloy powders after 2 h of milling was nearly 50 nm. After 3 h of milling, the crystallite size reduced below 36 nm.

It is known that most of the binary metallic systems in the AlNiCoFeCrTi HEA system possess limited solid solubility under equilibrium condition because of their positive heats of mixing. However, the six components MA powders with milling duration higher than 1 h show the formation of supersaturated bcc solid solution. The solid solubility extension is introduced by the effect of high mixing entropy (Murty et al. 2014; Tsai et al. 2014; Gao et al. 2016; Vaidya et al. 2019) and the non-equilibrium state of the MA process (Suryanarayana 2001; Vaidya et al. 2019). As the component number increases, the random diffusion between different elements will be enhanced and, thus, the solid solubility is extended. On the other hand, the MA process can also extend the solid solubility limits (Murty and Ranganathan 1998; Suryanarayana 2001; Suryanarayana et al. 2001; Vaidya et al. 2019). Alloying occurs when the grain/crystallite sizes of the elemental components decrease down to nanoscale and then a substantial amount of enthalpy can be stored in nanocrystalline alloy due to the large grain boundary area. The energy stored in the grain boundaries serves as the driving force for the formation of solid solution (Sui et al. 1992; Yeh et al. 2007a, b). Interdiffusion among the components occurs and the solid solubility is expected to increase with increase in milling time until it reaches a supersaturating level, beyond which no further extension of solid solubility will be achieved (Suryanarayana 2001; Vaidya et al. 2019).

It is known that the ball to powder interaction during high-energy ball milling involves continuous plastic deformation, fracture, and welding of particles finally leading to the nanocrystallization or even amorphization (Suryanarayana 2001; Suryanarayana et al. 2001; Vaidya et al. 2019). In the early period of MA process, the particles firstly are cold weld together to form even larger particles. The cold welded agglomerations are crushed down to smaller particles when the milling is prolonged. This circulation leads the powder be refined gradually and facilitates the diffusion and alloying among different metallic elements. The 3-h ball-milled alloy powder shows refined morphology with average particle size of 35 μm. Powder particles have irregular shape typically formed by MA technique (Suryanarayana 2001; Varalakshmi et al. 2010; Yurkova et al. 2016, 2019; Vaidya

et al. 2019). Compared to spherical shape indicative of gas-atomized powder, irregular shape of MA powder particles offers essential advantages, ensuring higher particle velocity as it was shown for cryomilled powder of Al alloy (Jodoin et al. 2006) and easier compaction under further consolidation in dense coating.

The results of quantitative elemental microanalysis on the EDX spectrum (not listed in this article) indicate that the homogeneity and equiatomic composition in each alloy particle after 3-h MA are not achieved.

Structure characterization of powder AlNiCoFeCrTi high-entropy alloy after annealing

It is well known that simple solid solution structures formed during MA are often metastable in nature and undergo phase transitions to different solid solution and complex phases on consolidation or heat treatment (Murty et al. 2014; Tsai et al. 2014; Gao et al. 2016; Vaidya et al. 2019). Figure 2b shows the XRD pattern of 3-h MA AlNiCoFeCrTi HEA after 1-h annealing at 1200 °C. A detailed analysis of the XRD pattern illustrates that the initial bcc solid solution is transformed into ordered bcc solid solution which was commonly designated as B2 phase (Murty et al. 2014; Gao et al. 2016). As a result, a new diffraction superlattice peak (100) at the angle $2\theta = 30.86$ was observed. In addition to the peaks for the ordered B2 solid solution, peaks for σ-phase (intermetallic FeCr compound) and TiC were also found in the X-ray diffraction spectrum; so, the alloy becomes three phased. The appearance of the diffraction peaks for ordered bcc (B2) phase and σ-phase is related to the phase decomposition of the metastable supersaturated bcc solid solution under heat treatment.
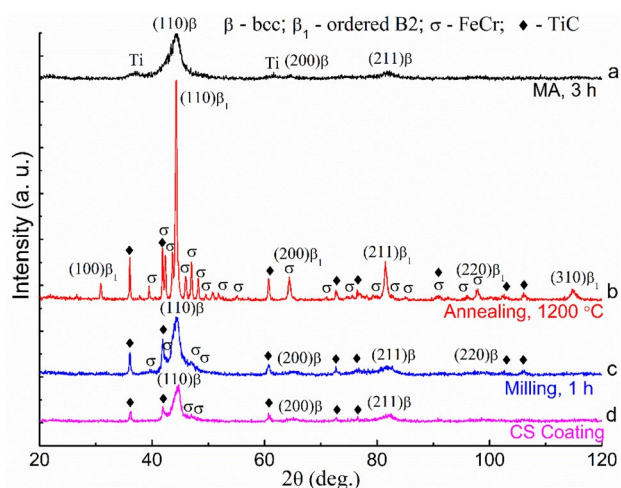

Fig. 2 XRD patterns of the AlNiCoFeCrTi high-entropy alloy powder after: 3-h MA (**a**); annealing for 1 h at temperature 1200 °C (**b**); 1-h milling (**c**); and AlNiCoFeCrTi CS coating (**d**)

B2 and σ phases are the most common intermetallic (IM) phase types in published HEAs (Tsai et al. 2019). Cr is an important constituent in HEAs, and as already discussed in the context of equiatomic alloys, Cr stabilizes the bcc structure and promotes formation of the σ-phase particularly in the presence of Fe, Co, and Ni (Murty et al. 2014). Hsu et al. indicated that σ-phase is likely to form for all chromium contents along with a B2 phase in $AlCoCrFeMo_{0.5}Ni$ HEA (Hsu et al. 2011).

The transformation from solid solutions to intermetallics is induced by the high negative mixing enthalpy between Ti and other elements (e.g., Fe, Ni, Co) (Jodoin et al. 2006).

In addition, as compared to a disordered bcc solid solution, the shift in the diffraction peaks for the ordered B2 phase towards smaller 2θ angles is observed (Fig. 3a, b), that indicates an increase in the parameter of the crystal lattice (Fig. 4), which is related to the release of the σ-phase, and the redistribution of Fe and Cr elements between the σ-phase and ordered B2 phase. The lattice parameter of the ordered B2 solid solution is 0.2895 nm.

The decrease in the width of the diffraction lines for the ordered B2 solid solution, and the increase in their intensity (Figs. 2, 3) indicate the decrease in the defect density for the crystal lattice, as well as the increase in the average size of crystallites due to the processes of returning and recrystallization that occur during annealing at temperature 1200 °C. Similar behavior had been also described in (Yurkova et al. 2016, 2019) for the AlCuNiFeCr and AlCuNiFeTi alloys prepared by MA.

The phase transformation under annealing temperature can be attributed to the metastable state of the supersaturated disordered bcc solid solution (Yurkova et al. 2016, 2019; Vaidya et al. 2019). This metastable structure transforms during annealing to more stable ordered bcc solid solution (B2 phase) and σ-phase. The ordered B2 phase
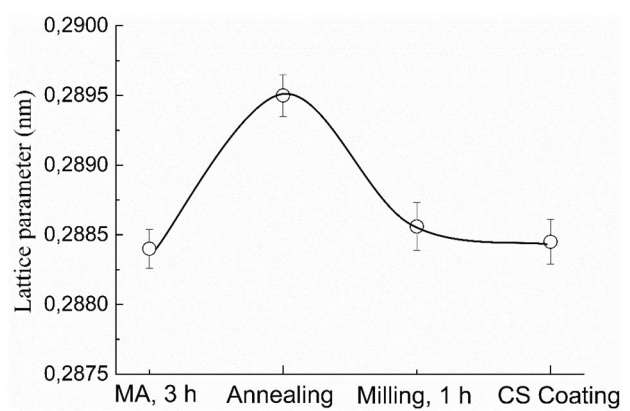

Fig. 4 Lattice parameters of AlNiCoFeCrTi HEA powder after 3-h MA, after annealing for 1 h at temperature 1200 °C, after 1-h milling, and AlNiCoFeCrTi CS coating

and σ-phase are the equilibrium phases, as the XRD analysis in Fig. 2b shows that annealing of the MA alloy at 1200 °C for 1 h results in their formation due to formation of metastable disordered bcc phase during MA (Fig. 2a) which is a non-equilibrium process.

The formation of TiC phase is associated with the high activity of Ti, which is not completely dissolved in bcc solid solution under MA (Fig. 2a), and as a result, during annealing residual pure Ti also reacts with carbon, which is a component of petrol used as a process controlling agent, that could be adsorbed in the closed pores formed during MA process.

Fig. 3 XRD detailed scans for the peak (110) of bcc and ordered bcc (**a**) and (211) of bcc and ordered bcc (**b**) of AlNiCoFeCrTi HEA powder after 3-h MA, after annealing for 1 h at temperature 1200 °C, after 1-h milling, and AlNiCoFeCrTi CS coating
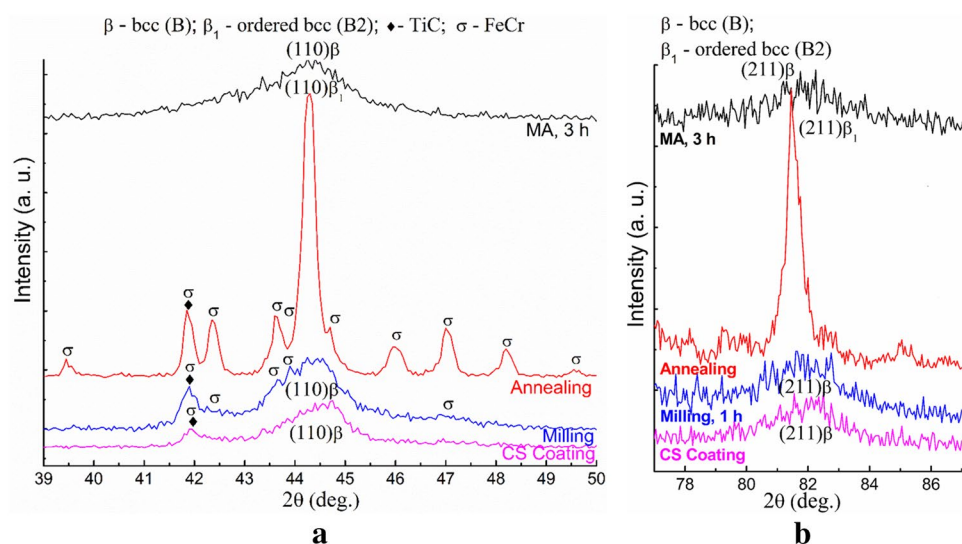
Phase evolution and microstructure of AlNiCoFeCrTi alloy after additional milling—characterization of feedstock powders

The powder agglomerates resulted from annealing at 1200 °C were grinded in a ball mill. The XRD pattern on Fig. 2c shows the phase transformation of AlNiCoFeCrTi high-entropy alloy after additional ball milling for 1 h. The additional milling would definitely affect the phase composition and lattice parameter of the formed solid solution. Unlike annealed powder (Fig. 3b), the peaks of disordered bcc solid solution and TiC are apparent. It can be seen that noticeable reduction of intensity is observed for bcc solid solution diffraction peaks. The diffraction peaks of σ-phase can hardly be seen in XRD pattern after the powder alloy has been ball milled for 1 h. In the process of additional milling, after annealing, a partial dissolution of σ-phase in bcc solid solution occurs, which is confirmed by a drastic decrease in the intensity of the corresponding peaks slightly on the left and right of the bcc phase in the XRD pattern (Fig. 2c) and bcc diffraction peaks shift to a higher angle as compared with post-annealing ordered B2 phase position on Fig. 2b. It can be seen in the enlarged image of XRD peaks around 44.5° (Fig. 3a) and 81.9° (Fig. 3b) that the diffraction peaks of bcc phase shift to the right side considerably after milling versus post-annealing. This phenomenon is associated with the contraction of crystal lattice, which is related with the variation of phase composition as the FeCr typed intermetallic σ-phase partially disappears in the AlNiCoFeCrTi alloy suggesting the enrichment of bcc phase by dissolved Fe and Cr, which atomic radii are smaller by than the atomic radii of Al and Ti. This dissolution is caused by enhanced diffusion under the impact of severe plastic deformation even at low milling temperature. Lattice parameter of bcc solid solution after 1-h milling decreases to 0.2885 nm and verges towards the value of this parameter after 3-h MA (Fig. 4). The mean crystallite size of the AlNiCoFeCrTi powders reaches 28 nm after additional 1 h of milling.

The morphology and microstructure of the feedstock AlNiCoFeCrTi HEA powders used for cold spraying coating are shown in Fig. 5a, b. The powder particles are irregular shaped with a size range of 1–125 μm (average powder size of 21 μm) as evident from the size distribution plot, shown in Fig. 5c.

A clear three-phase contrast is visible from SEM micrographs (Fig. 5b). Table 2 shows the composition analysis using spot EDX study on the three phases in AlNiCoFeCrTi powder. From the EDX study, volume fraction of the phases in the SEM and the phases present in the XRD pattern (Fig. 2c), it can be concluded that the gray phase is the major bcc solid solution, the light is σ-phase (intermetallic FeCr compound) and dark-gray phase is TiC.

The microhardness HV of the AlNiCoFeCrTi HEA in powder state after 1-h milling is 8.7 ± 0.4 GPa.

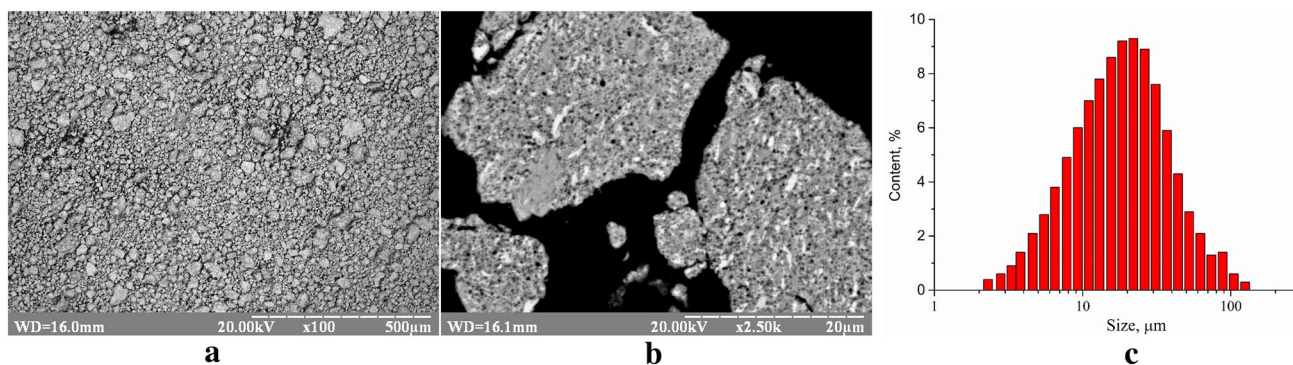This powder was used as feedstock powder for cold-spraying coatings.

Fig. 5 Morphology (**a**), microstructure (**b**) and particle size distribution (**c**) of the AlNiCoFeCrTi HEA powders after 1-h milling

	Phase	Al	Ni	Co	Fe	Cr	Ti	C	VEC, e/at	Name of phase
Table 2 SEM–EDX results of feedstock AlNiCoFeCrTi powder for cold spraying coatings (at. %)	Bulk/nominal	15.95	16.15	15.97	16.06	16.03	15.89	3.95	6.57	bcc
	Grey	21.27	16.82	16.93	13.94	13.85	14.72	2.47	6.48	bcc
	Light grey	7.38	10.04	11.94	31.43	28.57	8.49	2.15	–	σ
	Dark grey	3.58	2.29	3.81	3.88	4.74	39.47	42.23	–	TiC

Structure characterization of AlNiCoFeCrTi high-entropy cold-spraying coating

X-ray phase analysis results of the AlNiCoFeCrTi CS coating are shown in Fig. 3d. The diffraction peaks exhibit no change except for a minor broadening and an evident decline of diffraction intensity. The coatings consist of a disordered bcc solid solution, TiC and σ-phase. The XRD patterns shown in Fig. 3c, d reveal that both the AlNiCoFeCrTi HEA feedstock powder after 1-h milling and CS coatings has the same phase composition. No noticeable shift in bcc peaks is observed (Fig. 3), so the lattice parameter of bcc solid solution is not differing from that of after 1-h milling (Fig. 4). Due to the low processing temperature, no evidence of phase transformation and oxidation are observed in the HEA coatings, suggesting the maintenance of phase composition the same as that of feedstock AlNiCoFeCrTi powder. This is a unique advantage of CS process above other thermal spray processes (Wang et al. 2011; Dong et al. 2013; Cai et al. 2017a, b; Anupam et al. 2019). In addition, the intensity of the bcc, TiC and σ-phase diffraction peaks detected in the HEA coatings decreases and peaks are broadened than that in the 1-h milled HEA powder, indicating the possible occurrence of grain refinement and microstresses in the coatings due to the severe plastic deformation under CS process. Moreover, the diffraction peaks of σ-phase can hardly be seen on the XRD pattern shown in Fig. 3d. The mean crystallite size of bcc solid solution in the AlNiCoFeCrTi CS coating decreases to 24 nm as compared with feedstock powder before spraying.

The results of X-ray phase analysis of the coating are confirmed by data obtained via BSE-SEM and spot EDX analysis. Figure 6 shows typical cross-sectional BSE-SEM images of AlNiCoFeCrTi high-entropy alloy deposited by cold spray (CS) onto low carbon steel substrate. In AlNiCoFeCrTi CS coating, a clear three-phase contrast is seen in BSE-SEM micrographs, as well as in SEM images of the feedstock powder on Fig. 5b.

The AlNiCoFeCrTi coatings produced by CS are dense, relatively uniform, and adherent. As can be seen on low magnification images such as Fig. 6a, the mean thickness of the coating is about 450 μm but that this varies locally from around 430–470 μm due to the roughness of the coating surface and to the undulating coating/substrate interface. There are some small and large (≈5–20 μm across) dark features in the coating/substrate interface, which correspond to SiC particles which remained in the substrate surface after SiC blasting. Higher magnification SEM images such as Fig. 6b show that the coating/substrate interface is sufficiently abrupt and appear to be crack free. It can be observed that there is a good interface between AlNiCoFeCrTi coating and carbon steel substrate. Coating is rather dense with a porosity less than 1%, which is much lower than that of plasma-sprayed HEA coatings (7.4% ± 1.3%) (Ajdelsztajn et al. 2006; Zhang et al. 2011; Cai et al. 2017a, b; Anupam et al. 2019).

The evidences of metallurgical bonding commonly associated with impact fusion are also visible at the boundary of some adjacent particles, as shown in Fig. 6b. In addition, Fig. 6b shows evidence of overall plastic deformation and intense shear localisation at particle/particle boundaries. No cracking and delaminating are observed in as-sprayed coatings. SiC-blasting created deformed regions next to the surface of the substrate and interface between entrapped SiC particles and substrate.
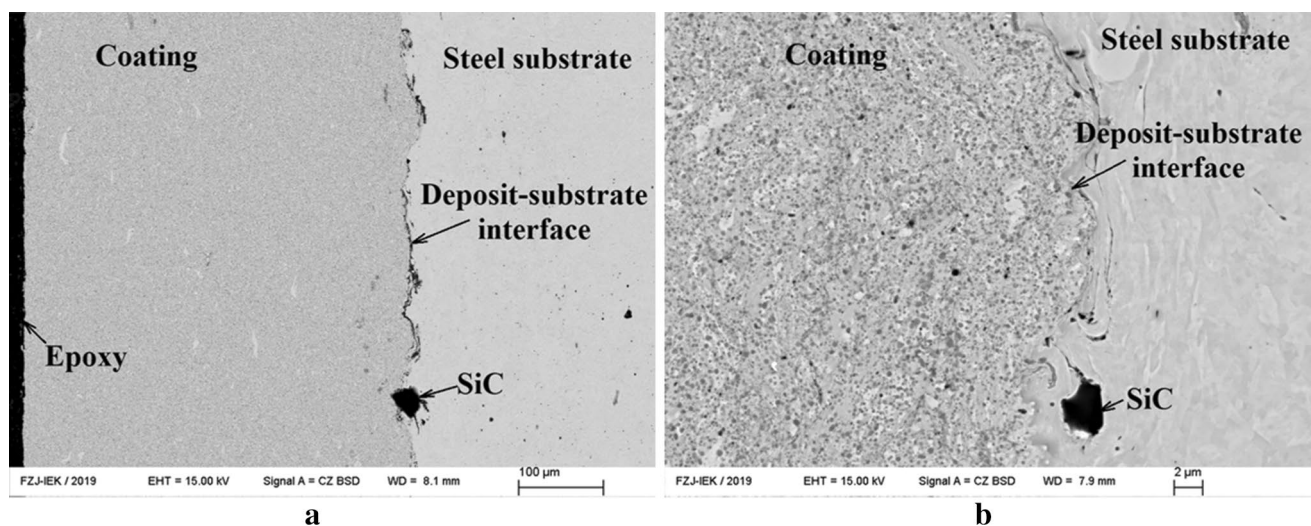

Fig. 6 Cross-sectional BSE-SEM micrographs of the AlNiCoFeCrTi cold-sprayed coatings: **a** low magnification image, and **b** higher magnification image

At the coating/substrate interface, 'inter-locking' phenomenon in the form of coating material mechanically trapped by the substrate material was observed. The formation of the 'interlocking' was due to the server plastic deformation of the soft low carbon steel substrate upon impact by the hard AlNiCoFeCrTi powder particles, and it can provide high adhesive strength to the coating/substrate interface. The deposition of the particles is mainly attributed to the deformation of powders themselves. Two different kinds of deformation ensure strong bonding at the particle/particle interfaces under cold spraying. Among them, severe plastic deformation of powder particles results in their flattening and mechanical interlocking the splats by cold forging under forward pressure (Stoltenhoff et al. 2002; Rokni et al. 2017; Yin et al. 2018a, b). Nevertheless, flow jet or adiabatic shear instability resulted from localized deformation at the particle boundaries is commonly believed to be primarily responsible for creating the mostly effective intimate metallic bonding between the adjacent particles under extremely high strain rate as a result of high impact velocity (Stoltenhoff et al. 2002; Assadi et al. 2003; Grujicic et al. 2004; Li et al. 2012; Rokni et al. 2017). Adiabatic interaction between particle/particle is based on the fact that the thermal diffusion distance is very small (in the order of 10^{-6} m) during the very short operational time of impact, i.e., 10^{-5} s (Grujicic et al. 2004; Ajdelsztajn et al. 2006; Li et al. 2012). This is
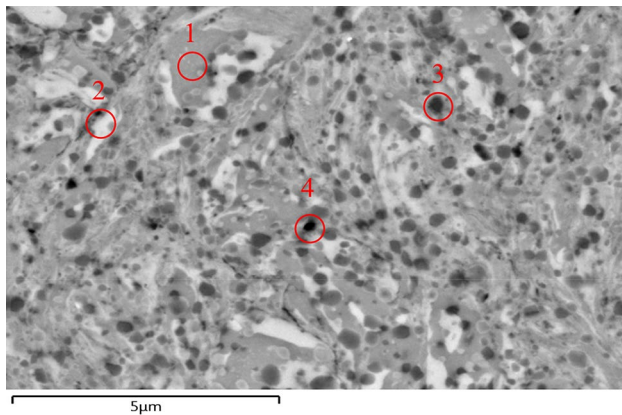
the reason of that why kinetic energy is mainly dissipated as heat, causing material softening and shear localization and promoting strong contact between two adjacent particles by mechanical interlocking and even by impact fusion, as evidenced from Fig. 6b.

Figure 7 represents microstructure of AlNiCoFeCrTi CS coating. A clear four-phase contrast is visible from SEM micrograph. Chemical composition of phases is shown in Table 3. The nominal composition of each element of alloy in this HEA changes from 15.30 to 15.76 at. %, and also recorded a low carbon and oxygen content that contaminated the material during MA and CS. From the BSE-SEM image and EDX results (Table 3), it is quite understandable that the phase indexed as gray (region 1) is an Al-rich phase. Fe, Cr and Ti are presented in the amount less than equiatomic levels. The phase labeled as light gray (region 2) is dominated by Fe and Cr with lesser amount of other elements in atomic percent. The phase labeled as dark gray (region 3) is containing Ti and C with the presence of low content of oxygen and other elements. Also in the microstructure of the coating, there is a black phase (region 4), which consists of aluminum and oxygen. From the EDX study, volume fraction of the phases in the SEM and the phases present in the XRD, it can be concluded that the gray phase (larger volume fraction) is the major bcc solid solution; this is also evidenced by the VEC value (Table 3). The light-gray phase is the small volume fraction of σ-phase (intermetallic FeCr compound) and dark-gray phase is TiC. Black region was formed as a result of the ingress of impurities (powder of aluminum oxide) from the spraying chamber into the coating during spraying. Content of black phase is negligible in the coating and as a result, these inclusions were not fixed with XRD analysis.

Microhardness of the AlNiCoFeCrTi alloy and coating

Figure 8 presents the microhardness values of the initial elements, AlNiCoFeCrTi alloy after 3-h MA, annealing, 1-h milling as well as the microhardness distribution from the surface to the interface of the CSed coating and steel substrate. The Vickers microhardness of the powder alloy

Fig. 7 Microstructure of the AlNiCoFeCrTi cold-sprayed coatings

Table 3 SEM–EDX results of the AlNiCoFeCrTi cold-sprayed coating

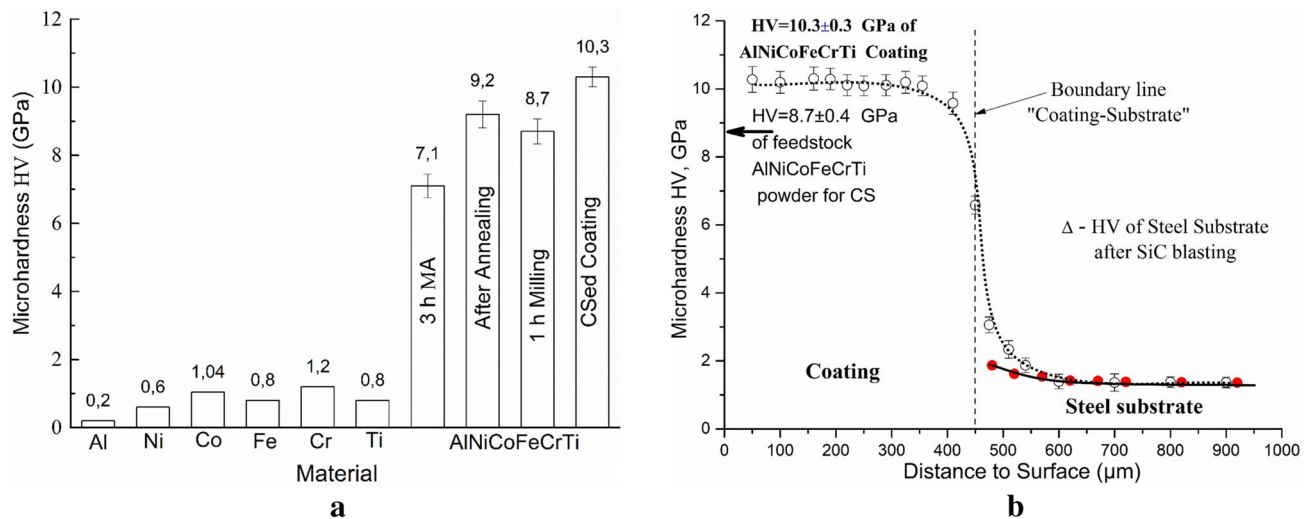| Phase		Concentration, at.%								KVE, e/at	Name of phase
		Al	Ni	Co	Fe	Cr	Ti	C	O		
Region	Bulk/nominal	15.30	15.65	15.61	15.76	15.53	15.49	3.67	2.98	6.57	bcc
1	Grey	20.97	16.31	16.12	14.03	14.54	12.88	2.84	2.31	6.47	bcc
2	Light gray	5.87	7.8	9.28	31.6	30.93	8.33	2.32	3.87	–	σ
3	Dark gray	4.75	3.11	2.87	4.22	5.05	42.16	34.31	3.53	–	TiC
4	Black	42.9	–	–	–	–	–	–	57.1	–	Al_2O_3

Fig. 8 Microhardness of **a** initial elements, AlNiCoFeCrTi alloy after 3-h MA, annealing at 1200 °C, 1-h milling, CSed coating and **b** microhardness profile along the cross section of the CSed AlNiCoFeCrTi coating

and coatings was measured with a load of 100 g. at room temperature.

As shown in Fig. 8a, the microhardness values of high-entropy AlNiCoFeCrTi alloy after 3-h MA are much higher than that of the initial components. Since no other phases besides bcc and residual Ti were detected in the alloy after MA, the microhardness enhancement to 7.1 GPa (equal to 710 HV) is likely attributed to the effect of Al and Ti with their larger atomic radii compared to the other components, which can contribute to an improved effect of solid solution strengthening and nanostructure strengthening mechanism of the alloy. An increase in the microhardness of the powder AlNiCoFeCrTi alloy after annealing to 9.2 ± 0.4 GPa is associated with phase transformation of bcc solid solution at high temperature, namely, with the formation of an ordered bcc solid solution (B2 phase) and precipitations of the hard intermetallic σ-phase as well as the formation of TiC. The AlNiCoFeCrTi alloy microhardness after additional 1-h ball milling drops to 8.7 ± 0.4 GPa (equal to 870 HV) because of phase transformation of ordered B2 phase into disordered bcc solid solution and decreasing the amount of σ-phase by its dissolution during the milling process. The Vickers microhardness of AlNiCoFeCrTi CSed coating has been found to be 10.3 ± 0.3 GPa (equal to 1030 HV) and is much higher than that of the feedstock powder due to densification, grain refining, as well as because of retaining the phase composition and nanostructured state combined with the effect of extremely high values of strain rate (in the order of $10^5 \ldots 10^7 \ s^{-1}$) sustained by powder particles under impact at the rather low processing temperature.

In addition, by comparing the microhardness of steel substrate before and after coating spraying (Fig. 8b), it can be noted the evident strain hardening of the steel substrate as a result of the effect of severe plastic deformation during the CS process.

Of importance remark is that as-received cold-sprayed AlNiCoFeCrTi coating exhibits the value of hardness higher than that for the HEA coatings prepared by laser cladding (Zhang et al. 2011; Cai et al. 2017a, b) and plasma spraying (Dong et al. 2013; Kumar et al. 2019), and also by CS reported in (Yin et al. 2018a, b; Anupam et al. 2019). This might be related to the coating composition, the feedstock powder production method as well as to the high-speed and rather low processing temperature of CS process.

Conclusions

In this study, solid-state MA and CS technologies were applied to produce AlNiCoFeCrTi HEA powder and coating from it, respectively. It has been shown that nanocomposite powder of AlNiCoFeCrTi alloy produced by MA and annealing can be used as the feedstock for cold spray deposition of nanostructured HEA coatings on the low carbon steel substrate.

A simple bcc solid solution and retained titanium, which is not completely dissolved in bcc phase because the largest atomic radius among the alloy components is obtained in the AlNiCoFeCrTi alloy by short-time mechanical alloying.

The bcc structure transforms to ordered B2 phase and σ-phase when the alloy is annealed at 1200 °C for 1 h. The phase transformation under annealing temperature is attributed to the formation of metastable supersaturated solid solution during MA which is a non-equilibrium process. In addition, TiC phase formation is a result of the reaction

between the retained Ti and carbon, which is a component of petrol, used as a process controlling agent.

The additional 1-h milling exhibits significant influence on phase composition and structure of as-annealed AlNi-CoFeCrTi alloy. The ordered B2 phase transforms into disordered bcc solid solution and σ-phase disappears partially, dissolving in bcc phase.

The coatings with mean thickness about 450 µm produced by CS process exhibit the same phase composition as the feedstock powder, i.e., the disordered bcc solid solution, σ-phase and TiC. The coatings are hard, dense, relatively uniform, and adherent with no evidence of interfacial debonding.

The microhardness of the CS AlNiCoFeCrTi coating reaches 10.3 GPa, which is much higher than most of the HEA coatings prepared by laser cladding and plasma spraying. The effect of solid solution strengthening, σ-phase and TiC particle hardening is additionally intensified by extremely high values of strain rate sustained by powder particles due to impact under cold spraying at the rather low processing temperature and plays crucial role in significant strain hardening of cold-sprayed coating. The high hardness proves the promising future of the CS coating.

References

Ajdelsztajn L, Zúñiga A, Jodoin B, Lavernia EJ (2006) Cold gas dynamic spraying of a high temperature Al alloy. Surf Coat Technol 201(6):2109–2116. https://doi.org/10.1016/j.surfcoat.2005.06.001

Alaneme KK, Bodunrin MO, Oke SR (2016) Processing, alloy composition and phase transition effect on the mechanical and corrosion properties of high entropy alloys: a review. J Mater Res Technol 5(4):384–393. https://doi.org/10.1016/j.jmrt.2016.03.004

Alkhimov AP, Papyrin AN, Kosarev VF et al (1994) Gas-dynamic spraying method for applying a coating. US Patent 5302414

Ang ASM, Berndt CC, Sesso ML et al (2014) Plasma-sprayed high entropy alloys: microstructure and properties of AlCoCrFeNi and MnCoCrFeNi. Metall Mater Trans A 46(2):791–800. https://doi.org/10.1007/s11661-014-2644-z

Anupam A, Kumar S, Chavan NM, Murty BS, Kottada RS (2019) First report on cold-sprayed AlCoCrFeNi high-entropy alloy and its isothermal oxidation. J Mater Res. https://doi.org/10.1557/jmr.2019.38

Assadi H, Gärtner F, Stoltenhoff T, Kreye H (2003) Bonding mechanism in cold gas spraying. Acta Mater 51(15):4379–4394. https://doi.org/10.1016/s1359-6454(03)00274-x

Cai Z, Cui X, Jin G, Liu Z, Li Y, Dong M (2017a) TEM observation on phase separation and interfaces of laser surface alloyed high-entropy alloy coating. Micron 103:84–89. https://doi.org/10.1016/j.micron.2017.10.001

Cai Z, Wang Y, Cui X, Jin G, Li Y, Liu Z, Dong M (2017b) Design and microstructure characterization of FeCoNiAlCu high-entropy alloy coating by plasma cladding: In comparison with thermodynamic calculation. Surf Coat Technol 330:163–169. https://doi.org/10.1016/j.surfcoat.2017.09.083

Chang Z-C (2018) Structure and properties of duodenary (TiVCrZrNbMoHfTaWAlSi)N coatings by reactive magnetron sputtering. Mater Chem Phys 220:98–110. https://doi.org/10.1016/j.matchemphys.2018.08.068

Dong Y, Lu Y, Kong J, Zhang J, Li T (2013) Microstructure and mechanical properties of multi-component AlCrFeNiMox high-entropy alloys. J Alloy Compd 573:96–101. https://doi.org/10.1016/j.jallcom.2013.03.253

Gao MC, Yeh J-W, Liaw PK, Zhang Y (2016) High-entropy alloys. Fundament Appl. https://doi.org/10.1007/978-3-319-27013-5

Grujicic M, Zhao C, DeRosset W, Helfritch D (2004) Adiabatic shear instability based mechanism for particles/substrate bonding in the cold-gas dynamic-spray process. Mater Des 25(8):681–688. https://doi.org/10.1016/j.matdes.2004.03.008

Guo S, Liu CT (2011) Phase stability in high entropy alloys: formation of solid-solution phase or amorphous phase. Progress Nat Sci Mater Int 21(6):433–446. https://doi.org/10.1016/s1002-0071(12)60080-x

Guo S, Ng C, Lu J, Liu CT (2011) Effect of valence electron concentration on stability of fcc or bcc phase in high entropy alloys. J Appl Phys 109(10):103505. https://doi.org/10.1063/1.3587228

Hsu C-Y, Juan C-C, Wang W-R, Sheu T-S, Yeh J-W, Chen S-K (2011) On the superior hot hardness and softening resistance of AlCoCrxFeMo05Ni high-entropy alloys. Mater Sci Eng A 528(10–11):3581–3588. https://doi.org/10.1016/j.msea.2011.01.072

Jodoin B, Ajdelsztajn L, Sansoucy E, Zúñiga A, Richer P, Lavernia EJ (2006) Effect of particle size, morphology, and hardness on cold gas dynamic sprayed aluminum alloy coatings. Surf Coat Technol 201(6):3422–3429. https://doi.org/10.1016/j.surfcoat.2006.07.232

Kumar A, Nayak SK, Bijalwan P, Dutta M, Banerjee A, Laha T (2019) Optimization of mechanical and corrosion properties of plasma sprayed low-chromium containing Fe-based amorphous/nanocrystalline composite coating. Surf Coat Technol 370:255–268. https://doi.org/10.1016/j.surfcoat.2019.05.010

Li Y, Wang X, Yin S, Xu S (2012) Influence of particle initial temperature on high velocity impact process in cold spraying. Proc Environ Sci 12:298–304. https://doi.org/10.1016/j.proenv.2012.01.281

Microtrac S3500 (2011) Tri-laser system, particle size analyser. https://www.microtrac.com. Accessed 28 June 2016

Miracle DB, Senkov ON (2017) A critical review of high entropy alloys and related concepts. Acta Mater 122:448–511. https://doi.org/10.1016/j.actamat.2016.08.081

Moridi A, Hassani-Gangaraj SM, Guagliano M, Dao M (2014) Cold spray coating: review of material systems and future perspectives. Surf Eng 30(6):369–395. https://doi.org/10.1179/1743294414y.0000000270

Murty BS, Ranganathan S (1998) Novel materials synthesis by mechanical alloying/milling. Int Mater Rev 43(3):101–141. https://doi.org/10.1179/imr.1998.43.3.101

Murty BS, Yeh J-W, Ranganathan S (2014) High-entropy alloys. Butterworth-Heinemann. https://doi.org/10.1016/C2013-0-14235-3

Papyrin A, Kosarev V, Klinkov S, Alkhimov A, Fomin V (2007) Cold spray technology. Elsevier Science, Novosibirsk

Pickering EJ, Jones NG (2016) High-entropy alloys: a critical assessment of their founding principles and future prospects. Int Mater Rev 61(3):183–202. https://doi.org/10.1080/09506608.2016.1180020

Raoelison RN, Xie Y, Sapanathan T, Planche MP, Kromer R, Costil S, Langlade C (2018) Cold gas dynamic spray technology: a comprehensive review of processing conditions for various technological developments till to date. Addit Manuf 19:134–159. https://doi.org/10.1016/j.addma.2017.07.001

Rokni MR, Nutt SR, Widener CA, Champagne VK, Hrabe RH (2017) Review of Relationship Between Particle Deformation, Coating Microstructure, and Properties in High-Pressure Cold Spray. J

Therm Spray Technol 26(6):1308–1355. https://doi.org/10.1007/s11666-017-0575-0

Stoltenhoff T, Kreye H, Richter HJ (2002) An analysis of the cold spray process and its coatings. J Therm Spray Technol 11(4):542–550. https://doi.org/10.1361/105996302770348682

Sui HX, Zhu M, Qi M, Li GB, Yang DZ (1992) The enhancement of solid solubility limits of AlCo intermetallic compound by high-energy ball milling. J Appl Phys 71(6):2945–2949. https://doi.org/10.1063/1.351028

Suryanarayana C (2001) Mechanical alloying and milling. Progr Mater Sci 46(1–2):1–184. https://doi.org/10.1016/s0079-6425(99)00010-9

Suryanarayana C, Ivanov E, Boldyrev V (2001) The science and technology of mechanical alloying. Mater Sci Eng A 304–306:151–158. https://doi.org/10.1016/s0921-5093(00)01465-9

Tsai M-H, Yeh J-W (2014) High-entropy alloys: a critical review. Mater Res Lett 2(3):107–123. https://doi.org/10.1080/21663831.2014.912690

Tsai M-H, Tsai R-C, Chang T, Huang W-F (2019) Intermetallic phases in high-entropy alloys: statistical analysis of their prevalence and structural inheritance. Metals 9(2):247. https://doi.org/10.3390/met9020247

Vaidya M, Muralikrishna GM, Murty BS (2019) High-entropy alloys by mechanical alloying: a review. J Mater Res 34(5):664–686. https://doi.org/10.1557/jmr.2019.37

Varalakshmi S, Kamaraj M, Murty BS (2010) Formation and stability of equiatomic and nonequiatomic nanocrystalline CuNiCoZnAlTi high-entropy alloys by mechanical alloying. Metall Mater Trans A 41(10):2703–2709. https://doi.org/10.1007/s11661-010-0344-x

Wang LM, Chen CC, Yeh J-W, Ke ST (2011) The microstructure and strengthening mechanism of thermal spray coating NixCo0.6Fe0.2CrySizAlTi0.2 high-entropy alloys. Mater Chem Phys 126(3):880–885. https://doi.org/10.1016/j.matchemphys.2010.12.022

Watson TJ, Nardi A, Ernst AT, Cernatescu I, Bedard BA, Aindow M (2017) Cold spray deposition of an icosahedral-phase-strengthened aluminum alloy coating. Surf Coat Technol 324:57–63. https://doi.org/10.1016/j.surfcoat.2017.05.049

Ye YF, Wang Q, Lu J, Liu CT, Yang Y (2016) High-entropy alloy: challenges and prospects. Mater Today 19(6):349–362. https://doi.org/10.1016/j.mattod.2015.11.026

Yeh J-W, Chang S-Y, Hong Y-D, Chen S-K, Lin S-J (2007a) Anomalous decrease in X-ray diffraction intensities of Cu–Ni–Al–Co–Cr–Fe–Si alloy systems with multi-principal elements. Mater

Chem Phys 103(1):41–46. https://doi.org/10.1016/j.matchemphys.2007.01.003

Yeh J-W, Chen YL, Lin SJ, Chen SK (2007b) High-entropy alloys—a new era of exploitation. Mater Sci Forum 560:1–9. https://doi.org/10.4028/www.scientific.net/msf.560.1

Yin S, Cavaliere P, Aldwell B, Jenkins R, Liao H, Li W, Lupoi R (2018a) Cold spray additive manufacturing and repair: fundamentals and applications. Addit Manuf 21:628–650. https://doi.org/10.1016/j.addma.2018.04.017

Yin S, Li W, Song B et al (2018b) Deposition of FeCoNiCrMn high entropy alloy (HEA) coating via cold spraying. J Mater Sci Technol. https://doi.org/10.1016/j.jmst.2018.12.015

Yurkova AI, Chernyavskii VV, Gorban VF (2016) Structure and mechanical properties of high-entropy AlCuNiFeTi and AlCuNiFeCr alloys produced by mechanical activation followed by pressure sintering. Powder Metall Met Ceram 55(3–4):152–163. https://doi.org/10.1007/s11106-016-9790-3

Yurkova AI, Cherniavsky VV, Bolbut V, Krüger M, Bogomol I (2019) Structure formation and mechanical properties of the high-entropy AlCuNiFeCr alloy prepared by mechanical alloying and spark plasma sintering. J Alloy Compd 786:139–148. https://doi.org/10.1016/j.jallcom.2019.01.341

Zhang H, Pan Y, He Y-Z (2011) Synthesis and characterization of FeCoNiCrCu high-entropy alloy coating by laser cladding. Mater Des 32(4):1910–1915. https://doi.org/10.1016/j.matdes.2010.12.001

Zhang S, Wu CL, Yi JZ, Zhang CH (2015) Synthesis and characterization of FeCoCrAlCu high-entropy alloy coating by laser surface alloying. Surf Coat Technol 262:64–69. https://doi.org/10.1016/j.surfcoat.2014.12.013

Zhang W, Tang R, Yang ZB et al (2018) Preparation, structure, and properties of high-entropy alloy multilayer coatings for nuclear fuel cladding: a case study of AlCrMoNbZr/(AlCrMoNbZr) N. J Nucl Mater 512:15–24. https://doi.org/10.1016/j.jnucmat.2018.10.001

Zhang Y, Zhou YJ, Lin JP, Chen GL, Liaw PK (2008) Solid-Solution Phase Formation Rules for Multi-component Alloys. Adv Eng Mater 10(6):534–538. https://doi.org/10.1002/adem.200700240

Publisher's Note Springer Nature remains neutral with regard to jurisdictional claims in published maps and institutional affiliations.